

Research Article

Magnetohydrodynamic Simulations of Hypersonic Flow over a Cylinder Using Axial- and Transverse-Oriented Magnetic Dipoles

Andrew N. Guarendi and Abhilash J. Chandy

Department of Mechanical Engineering, The University of Akron, Akron, OH 44325-3903, USA

Correspondence should be addressed to Abhilash J. Chandy; achandy@uakron.edu

Received 13 August 2013; Accepted 15 September 2013

Academic Editors: P.-C. Chen and K. M. Isaac

Copyright © 2013 A. N. Guarendi and A. J. Chandy. This is an open access article distributed under the Creative Commons Attribution License, which permits unrestricted use, distribution, and reproduction in any medium, provided the original work is properly cited.

Numerical simulations of magnetohydrodynamic (MHD) hypersonic flow over a cylinder are presented for axial- and transverse-oriented dipoles with different strengths. ANSYS CFX is used to carry out calculations for steady, laminar flows at a Mach number of 6.1, with a model for electrical conductivity as a function of temperature and pressure. The low magnetic Reynolds number ($\ll 1$) calculated based on the velocity and length scales in this problem justifies the quasistatic approximation, which assumes negligible effect of velocity on magnetic fields. Therefore, the governing equations employed in the simulations are the compressible Navier-Stokes and the energy equations with MHD-related source terms such as Lorentz force and Joule dissipation. The results demonstrate the ability of the magnetic field to affect the flowfield around the cylinder, which results in an increase in shock stand-off distance and reduction in overall temperature. Also, it is observed that there is a noticeable decrease in drag with the addition of the magnetic field.

1. Introduction

Space agencies including NASA have been currently engaged in research to develop low-cost alternatives for access-to-space and novel concepts for high Mach number or hypersonic propulsion. Hypersonic vehicles require essential improvements in order to ensure economic viability and to fulfill mission and safety constraints. For the last two decades various methods have been investigated to control hypersonic air flows specifically with regard to (a) lowering heat transfer to high-speed flying bodies, (b) inlet flow optimization in scramjets, (c) wave drag and wave turbulence cancellation, and (d) braking for atmospheric reentry. More recently there has been an intense interest in using MHD techniques to control the flow, and their potential applications are aimed at improving the performance during off-design conditions [1]. Besides the use of plasmas in space thrusters, a growing interest is evident in plasma-based aerodynamics, including flow manipulation through MHD forces, and drag reduction [2–6]. The size and complexity of this problem have led to

growing importance of numerical methods for design and optimization, especially due to the difficulties of reproducing the MHD interactions around a hypersonic vehicle in laboratory test facilities. Recent developments in Computational Fluid Dynamics (CFD) such as increased robustness of CFD codes, lower computational costs, and improvements in hardware as well as grid generation and more user-friendly postprocessing tools can reduce dramatically the design and development time required for new vehicles.

Magnetohydrodynamics (MHD) concerns the flows of electrically conducting fluids in the presence of a magnetic field. These flows obey the coupled Navier-Stokes (NS) and Maxwell equations and are accompanied by the occurrence of induced electric currents within the fluid, which leads to Joule dissipation [7]. The suppression of motion of these fluids by a static magnetic field is a subject of increasing interest in many technologies [7, 8] including aerospace. In such MHD applications, the magnetic Reynolds number $Re_m = UL/\eta \ll 1$ (U and L are velocity and length scales, resp., and η is the magnetic diffusivity). At low Re_m , one can invoke the

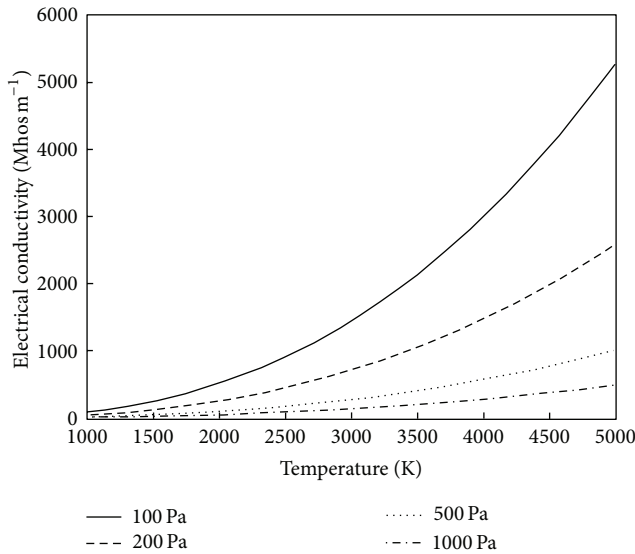


FIGURE 1: Electrical conductivity versus temperature for various pressures.

quasistatic approximation in MHD, where the influence of the velocity field on MHD is assumed to be negligible.

Some of the earliest works included [9–12]. Later, Coakley and Porter [13] developed the first CFD simulations of an MHD blunt body problem, though with simplifications in order to reduce computational effort. In the late 1990s and early 2000s, interest in MHD effects began to spring anew, as materials research began catching up and further demand for increased capability in space by both national and commercial entities emerged [14–17]. Furthermore, the revelation of a Soviet hypersonic plane—the AJAX project—demonstrated for the first time a potential real-world application of hypersonic MHD flow control. This work on MHD hypersonic flow was continued by many researchers [18–21], who conducted both physical experiments and computational methods for hypersonic MHD flow over blunt bodies. More recently, Grigoriadis et al. [22] computed hypersonic MHD flow past a cylinder using the immersed boundary method. Bisek et al. [23] investigated the effects of a magnetic field on hypersonic flow using variable electrical conductivity models and an argon gas medium in considering its application as a heat shield for reentry vehicles. Over the last few years, development of hypersonic MHD applications has begun to cluster into flow control, hypersonic inlets, and power generation [24–26]. For instance, depending on the orientation and magnitude of the magnetic field, drag can be either increased or decreased around a cylinder, [22, 27, 28] and the location of the shock wave can be altered, potentially dissipated, or even eliminated [29].

In this era of the retirement of the Space Shuttle, the growth of space programs around the world, and the emergence of commercial entities such as SpaceX (<http://www.spacex.com/>), MHD looks to play an ever increasing role in the future of aerospace. This paper examines hypersonic laminar flow of partially ionized air over a cylinder with an

applied magnetic field in the form of a dipole oriented in the axial and transverse directions. Particular focus is given to the resulting change in flow patterns, heat transfer, and drag forces.

2. Formulation

The governing equations solved in this study are the compressible Navier-Stokes equations along with the magnetic effects in the form of the Lorentz force in the momentum equation and the Joule dissipation term in the energy equation. With the steady-state assumption, the equations are given by

$$\begin{aligned} \nabla \cdot (\rho \mathbf{U}) &= 0, \\ \nabla \cdot (\rho \mathbf{U} \otimes \mathbf{U}) &= -\nabla p + \nabla \cdot \boldsymbol{\tau} + F_{\text{Lor}}, \\ \nabla \cdot (\rho \mathbf{U} h_{\text{tot}}) &= \nabla \cdot (\lambda \nabla T) + \nabla \cdot (\mathbf{U} \cdot \boldsymbol{\tau}) + J_H, \end{aligned} \quad (1)$$

where the stress tensor $\boldsymbol{\tau}$ is related to the strain rate by

$$\boldsymbol{\tau} = \mu \left(\nabla \mathbf{U} + (\nabla \mathbf{U})^T - \frac{2}{3} \delta \nabla \cdot \mathbf{U} \right). \quad (2)$$

3. Problem Description

The problem studied consists of the flow of partially ionized air over a cylinder at hypersonic speeds. The flow is assumed to be laminar and steady with a reference pressure of 85 Pa. The medium is treated as an ideal gas, with no chemical equilibrium or real gas effects. The inlet velocity is 2088.6 m/s at a temperature of 291.44 K and a Mach number of 6.1. The viscosity was adjusted so as to have the calculated Reynolds number for this flow as

$$\text{Re} = \frac{\rho U L}{\mu} \approx 234. \quad (3)$$

These far-field temperature and pressure values are those of air at an altitude of 50,000 m [30].

A constant magnetic field is applied and is modeled as a dipole centered at the center of the cylinder. However, the dipole is essentially treated as a 2D model completely independent of the z -direction coordinates. The ideal dipole field employed in this study is given by [23]

$$\mathbf{B} = \frac{-B_{\text{max}}}{2(x^2 + y^2)^{5/2}} \begin{bmatrix} 2x^2 - y^2 \\ 3xy \\ 0 \end{bmatrix}. \quad (4)$$

4. Computational Details

The simulations are performed using the commercial CFD code, ANSYS CFX. The computational domain consists of a cylinder with diameter, D_c , enclosed by a second cylinder with a diameter of $40D_c$. The domain extends along the cylindrical axis for a length of $2D_c$. The mesh contains 201,000 elements uniformly biased towards the center cylinder. The entrance region, that is, the inlet is specified as an “inlet” boundary condition, the outflow region a “supersonic outlet,”

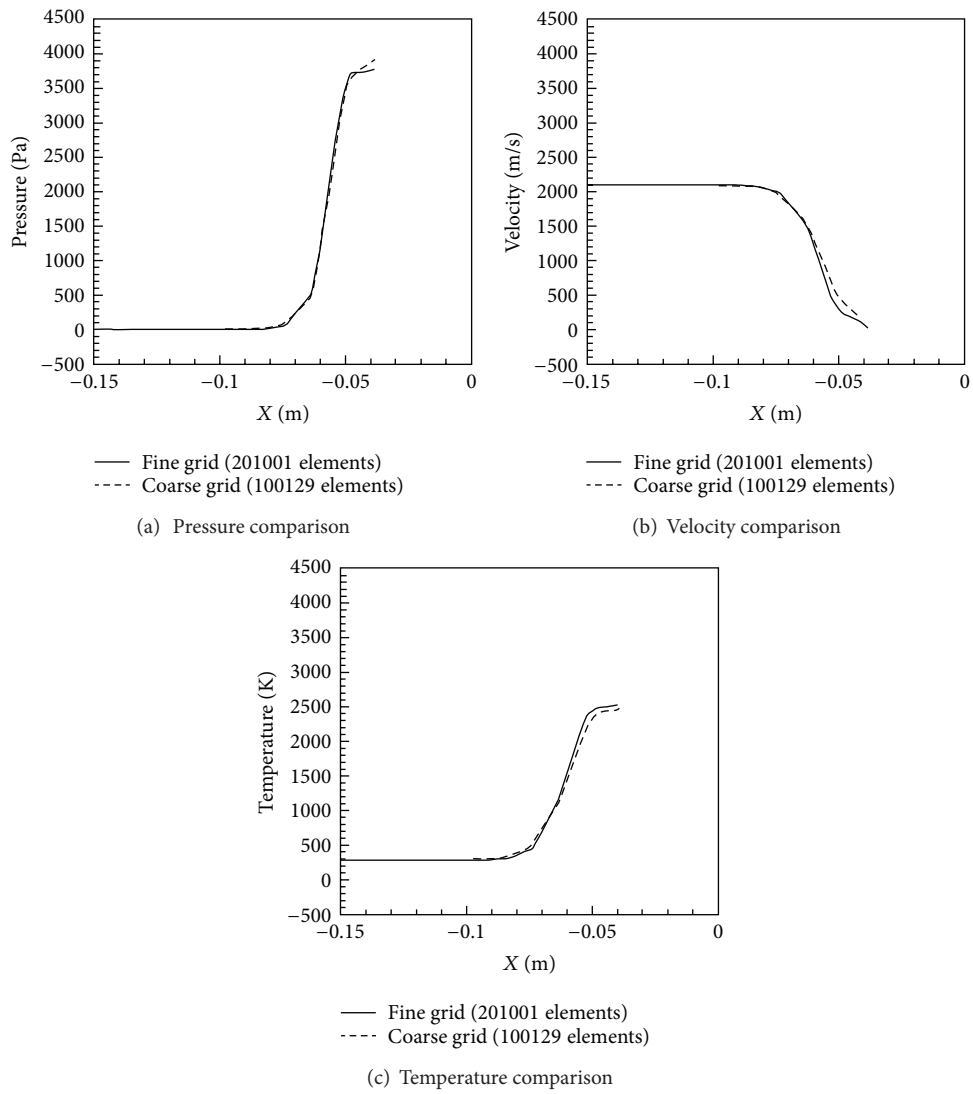


FIGURE 2: Grid independence comparison.

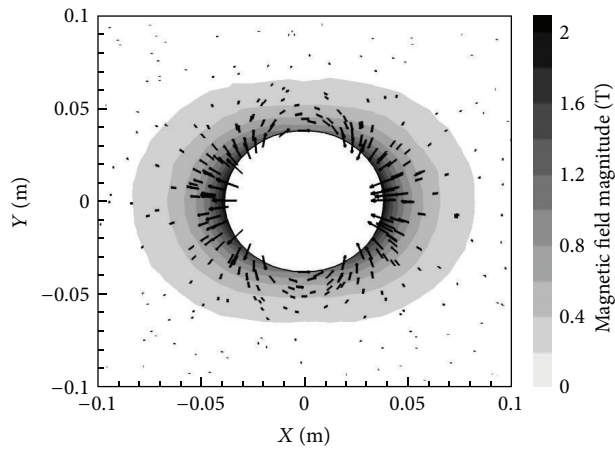


FIGURE 3: Magnetic field vectors and contours of the magnitude for an X -oriented dipole with $B_{\max} = 2$ T.

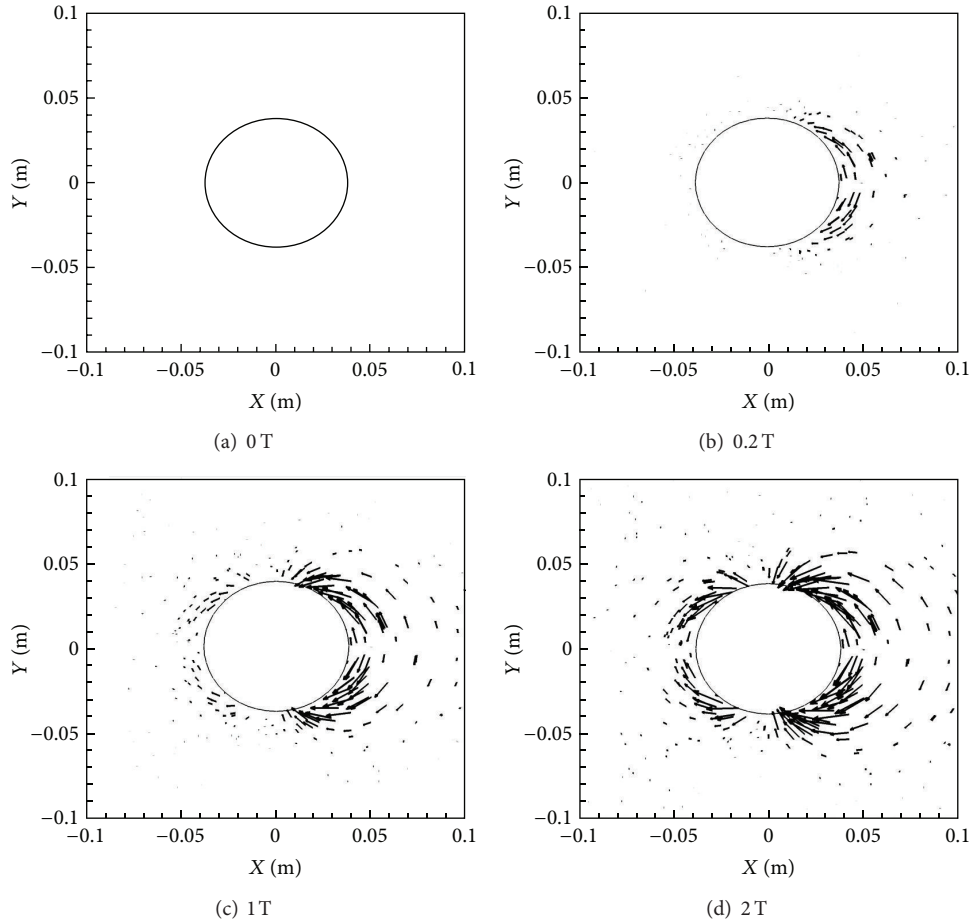


FIGURE 4: Lorentz force vectors for various B_{\max} with X-orientation.

and the two sides of the domain in the z -direction are assigned the “symmetry” boundary condition. The wall of the cylinder itself is considered to be “adiabatic” and “nonconducting.”

As mentioned above steady state was assumed. For viscosity and thermal conductivity, a Sutherland’s model was used. Electrical conductivity was derived based on the Chapman-Enskog model and is dependent on pressure and temperature, details of which are provided below.

Under the low- Re_m assumption defined by

$$Re_m = \sigma \mu_o UL \approx 0.001, \quad (5)$$

we can neglect any induced magnetic fields and treat the magnetic field as constant [31]. This allows us to also simplify our set of equations and condense the MHD effects into a source term in the momentum and energy equations, which are the Lorentz force and Joule heat terms, respectively.

4.1. Electrical Conductivity. For electrical conductivity, the Chapman-Enskog method [32] was implemented. This method of calculating electrical conductivity is given by

$$\sigma = \frac{3 n_e e^2}{4 m_e} \frac{1}{\sqrt{8kT/\pi m_e}} \frac{1}{nQ}, \quad (6)$$

where Q , the momentum transfer cross-section of collision, is

$$Q = 4.398 \times 10^{-10} \frac{\ln(\Lambda)}{T^2}, \quad (7)$$

Λ is a parameter equal to the ratio of the Debye shielding distance to the impact parameter for 90-degree scattering by an ion and is given by

$$\Lambda = 3 \left(\frac{1}{\epsilon_0} \frac{n_s e^2}{kT} \right)^2 \left(\frac{4\pi\epsilon_0}{e^2} \right) kT, \quad (8)$$

and the number density of air, n , is

$$n = \frac{N_A}{M_{\text{air}}} \rho, \quad (9)$$

which after employing the ideal gas law can be expressed as

$$n = \frac{N_A}{M_{\text{air}}} \frac{P}{R_{\text{air}} T}. \quad (10)$$

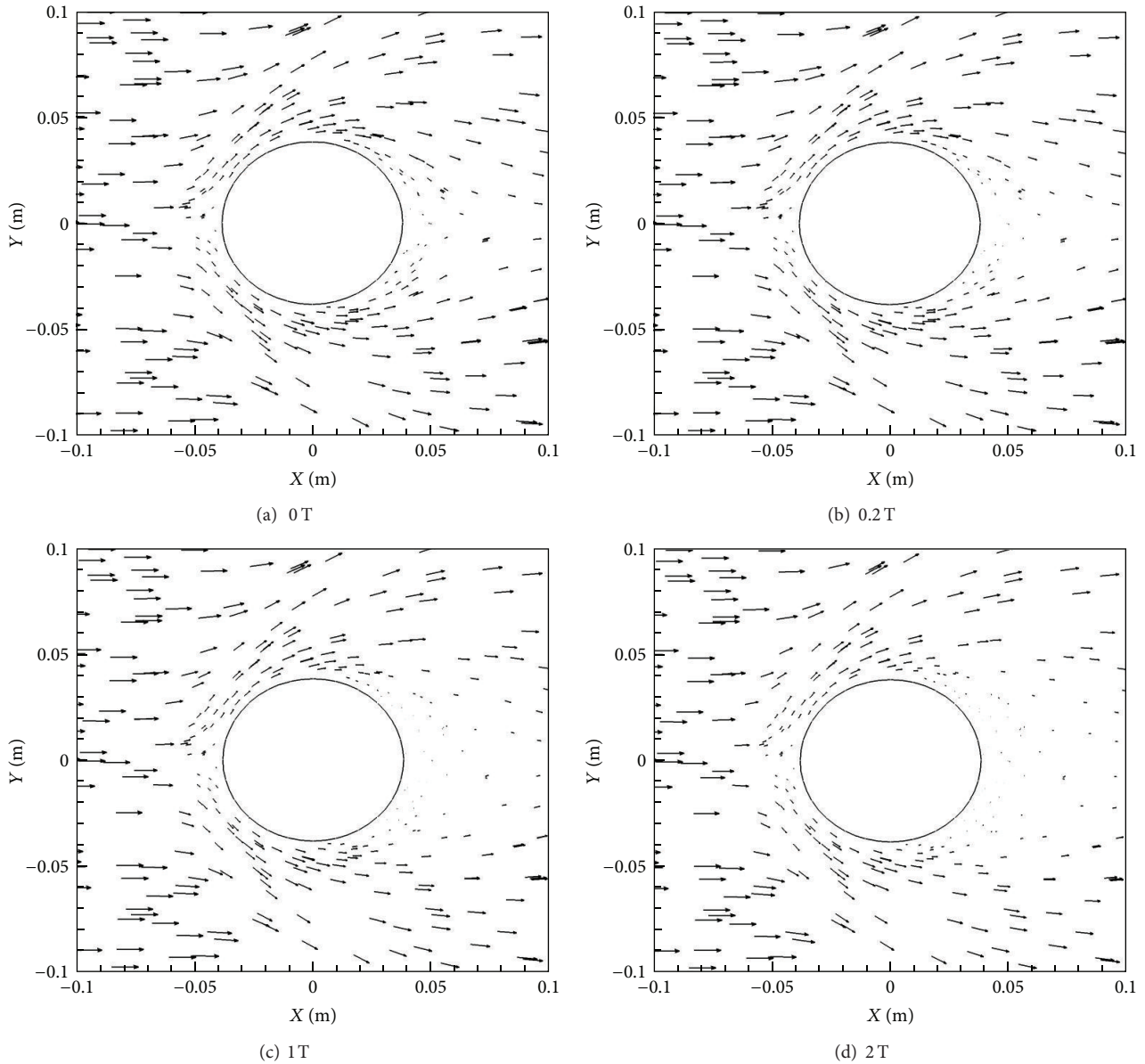


FIGURE 5: Velocity vectors for various B_{max} with X-orientation.

More details can be found in [32]. In these equations, m_e is the electron mass ($=9.10938 \times 10^{-31}$ kg), e is the electric charge ($=1.6022 \times 10^{-19}$ Coulombs), k is Boltzmann's constant ($=1.38065 \times 10^{-23}$ J/K), ϵ_0 is the permeability of free space ($=1.25664 \times 10^{-6}$ m·kg/s² A²), N_A is the Avogadro constant ($=6.02214 \times 10^{23}$ mol⁻¹), M_{air} is the molar mass of air ($=.02897$ kg/mol), R_{air} is the specific gas constant for air ($=287.04$ J/kg K), and n_e is the electron number density. We assume a constant electron density value of $n_e = 10^7$ cm⁻³ from electron beam ionization throughout the flowfield, which corresponds to weakly ionized airflow [33, 34]. The resulting model, which is the solution of (6)–(10), is dependent on only temperature and pressure. Figure 1 demonstrates the increase in electrical conductivity that comes with both an increase in temperature and a decrease in pressure.

5. Grid Independence

To ensure that the results are grid independent, calculations from the fine mesh of 201,000 elements were compared with those from a second, coarse mesh with 100,000 elements (see Figure 2). These were carried out in the absence of any magnetic field. In comparing the drag coefficients for the two meshes, a resulting error of 0.24% was obtained between the two meshes.

6. Results

In this section, results from simulations of hypersonic flow over a cylinder are presented. Parametric studies include two different kinds of orientations, X- and Y-oriented dipoles,

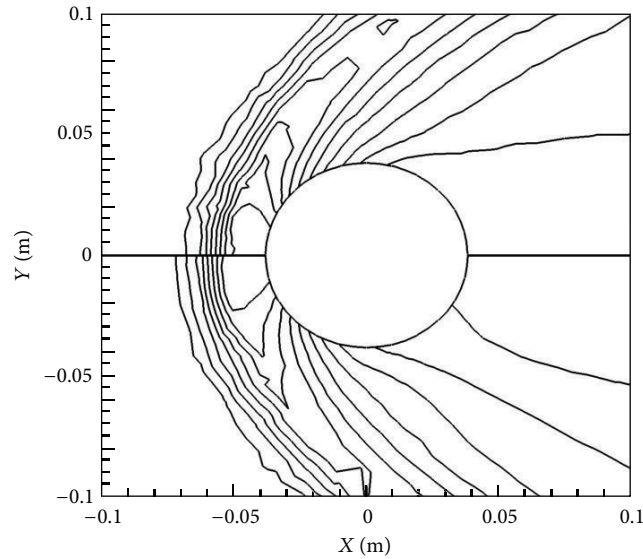


FIGURE 6: Comparison of density contours without magnetic field (top) and with $B_{\max} = 2$ T oriented in X-direction (bottom).

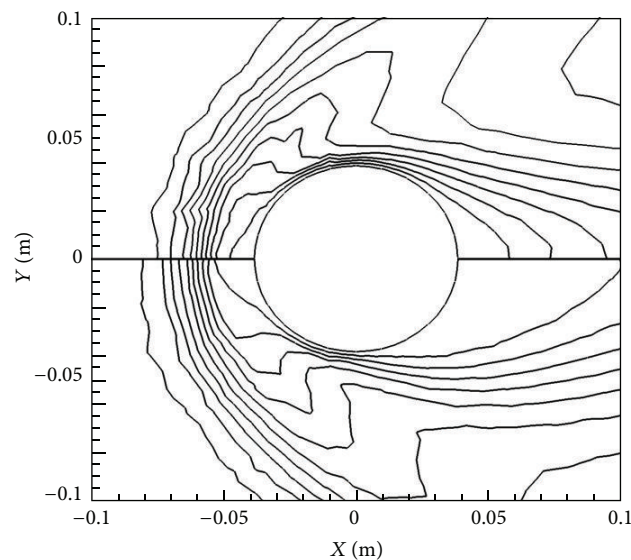


FIGURE 7: Comparison of U velocity contours without magnetic field (top) and with $B_{\max} = 2$ T oriented in X-direction (bottom).

and four different magnetic field strengths, with $B_{\max} = 0$ T, 0.2 T, 1.0 T, and 2.0 T. Analysis includes comparisons of velocity, temperature, Lorentz force, and Joule heat.

6.1. X-Oriented Magnetic Field. Equation (4) gives the magnetic field dipole oriented in the X-direction. The negative sign in front of B_{\max} implies that the flux vectors are oriented in the negative X-direction.

Figure 3 presents the magnetic field vectors according to the X-oriented dipole and also contours showing the magnitude of the magnetic field itself, calculated as $|B| = \sqrt{B_x^2 + B_y^2}$.

Figure 4 shows the Lorentz force vectors for the four different magnetic field cases, that is, $B_{\max} = 0, 0.2, 1.0,$ and 2.0 T. From these figures it is evident that the Lorentz forces are

larger behind the cylinder compared to the front in all the cases, with the effects in the front subsequently increasing with B_{\max} . The Lorentz force is directly proportional to magnetic field, B , current density, J , and electrical conductivity, σ . While B is symmetric across the front and back, σ is considerably larger behind the cylinder compared to the front as a result of higher temperatures and lower pressures. This in turn causes the J to be bigger in these regions as well, making the Lorentz force effects more significant behind the cylinder.

Figure 5 presents the velocity vectors for the same four cases. It can be observed that, with an increase in magnetic field from 0 T to 2.0 T, the velocity is considerably slowed down, especially behind the cylinder due to the damping effect of the Lorentz force. Since the Lorentz forces are larger behind the cylinder due to the reasons mentioned

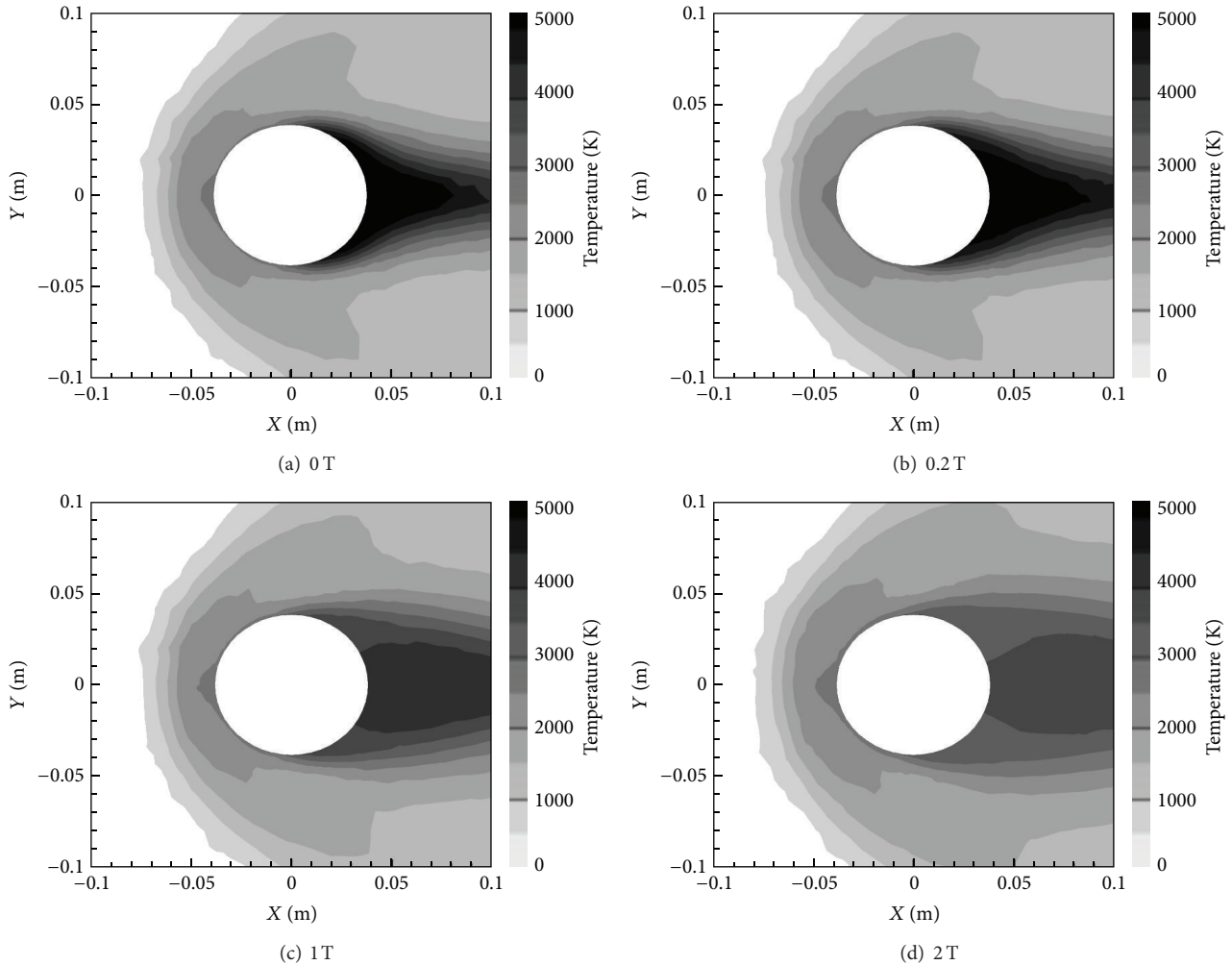


FIGURE 8: Temperature contours for various B_{max} with X-orientation.

above, velocity is influenced much more behind the cylinder compared to the front.

The effect that the Lorentz force has on the flow is clearly demonstrated in Figures 6 and 7, where density and velocity contours are shown for the lowest and highest magnetic field cases, that is, $B_{max} = 0$ T and $B_{max} = 2.0$ T on top and bottom. There is a marked reduction in velocity immediately around the cylinder, especially behind it, for the 2.0 T case, as the flowlines are pushed out further from the cylinder. The same kind of effect is also noticeable in the density contours in Figure 6 as the shock location moves away from the cylinder towards the front with the addition of the magnetic field.

Figure 8 shows the temperature contours of the four magnetic field cases of the X-oriented dipole. These contours also show a change, as with increasing B_{max} comes a reduction in overall wall-adjacent temperature around the cylinder. More specifically, the temperature around the cylinder tends towards more uniformity with an increasing magnetic field. This is because the Lorentz force that dampens the flow also reduces the convection heat transfer effects, thereby making

conduction more dominant and temperature more uniform [11, 14].

At the same time, however, Joule heat increases with B_{max} as shown in Figure 9. This figure presents the Joule heat contours in the entire domain for the different cases. Joule heat is calculated as J^2/σ , where J is the current density magnitude. Subsequently, in Figure 9 the Joule heat is considerably higher in those areas with both a higher current density, J , and a relatively lower electrical conductivity, σ . The electrical conductivity is the highest right behind the cylinder and right in front of the cylinder due to higher temperatures and/or lower pressures. Every other region around the cylinder has a lower electrical conductivity. Furthermore, since the magnetic field is X-oriented, the current density is the highest in an X-oriented elliptical region around the cylinder. These two factors determine the distribution of Joule heat pattern shown in Figure 9. Although Joule heat does lead to an increase in the temperature of the flow, it is overcome by the reduction in temperature around the cylinder due to Lorentz force effects.

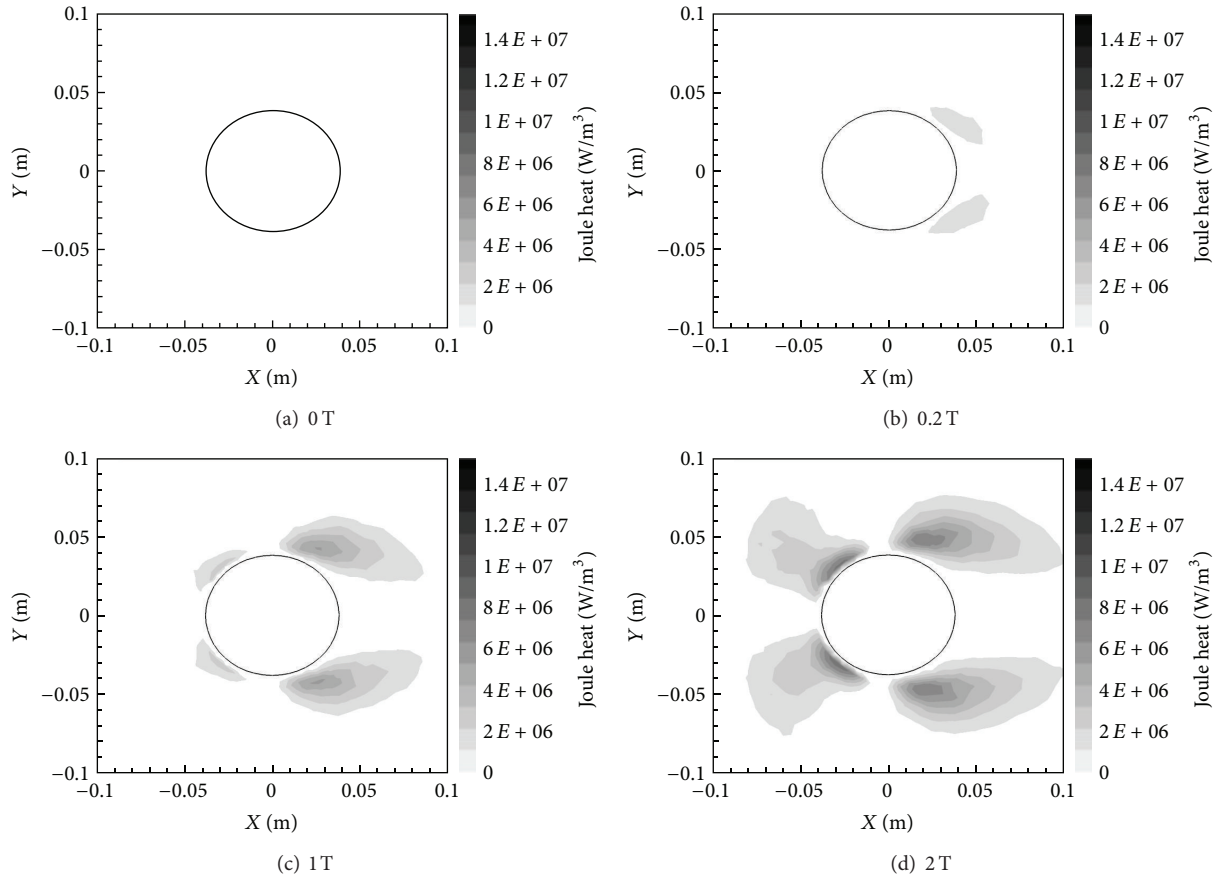


FIGURE 9: Joule heat contours for various B_{\max} with X-orientation.

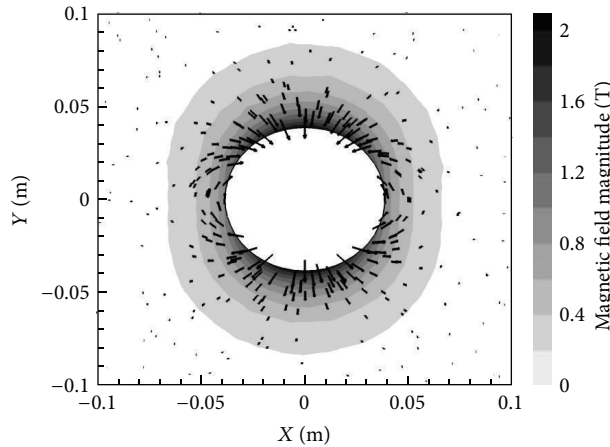


FIGURE 10: Magnetic field vectors and contours of the magnitude for a Y-oriented dipole with $B_{\max} = 2$ T.

6.2. *Y-Oriented Magnetic Field.* This section presents results from MHD simulations of electrically conducting flow around a cylinder, where the magnetic field of different strengths is generated using a Y-oriented dipole, with the rest of the boundary conditions being exactly the same as in the previous section. Figure 10 shows the contours of magnetic field strength along with the magnetic field vectors. Again,

due to the direction of magnetic flux, the magnetic field vectors are oriented in the negative y -direction.

Figure 14 shows the Lorentz force vectors for the four Y-oriented magnetic dipole cases of $B_{\max} = 0$ T, 0.2 T, 1 T, and 2 T. The Lorentz force is primarily oriented along the top and bottom of the cylinder. This is expected since the magnetic field has its maximum strength in these regions.

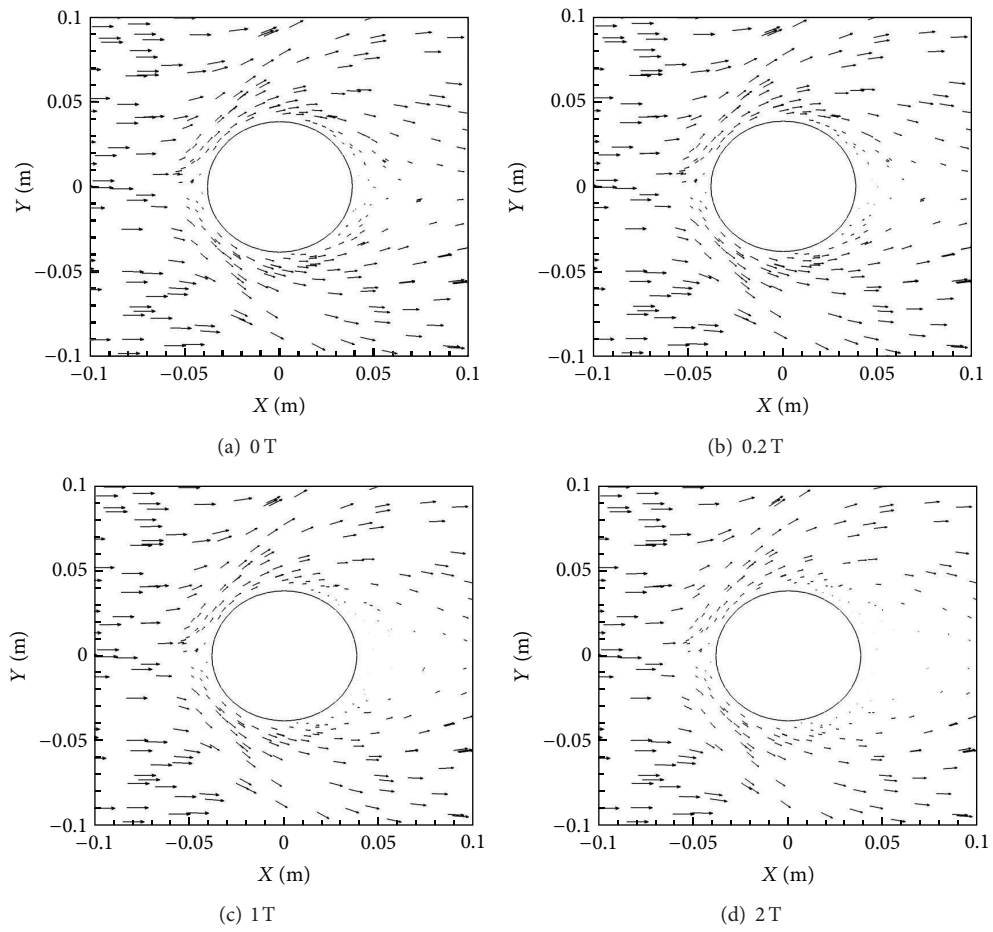


FIGURE 11: Velocity vectors for various B_{\max} with Y -orientation.

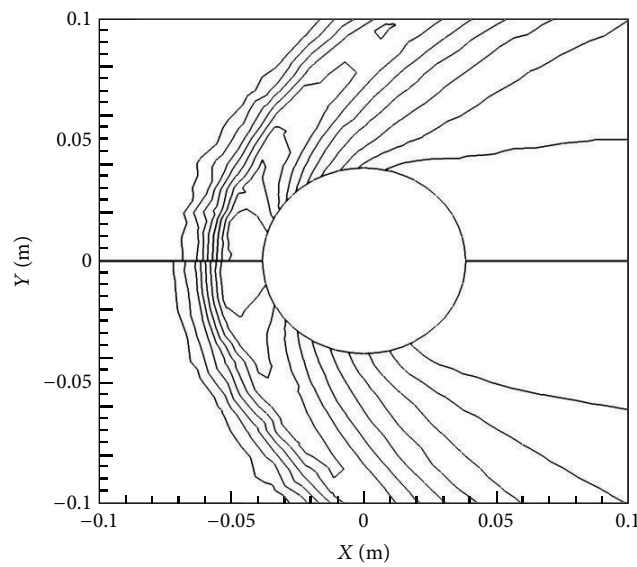


FIGURE 12: Comparison of density contours without magnetic field (top) and with $B_{\max} = 2$ T oriented in Y -direction (bottom).

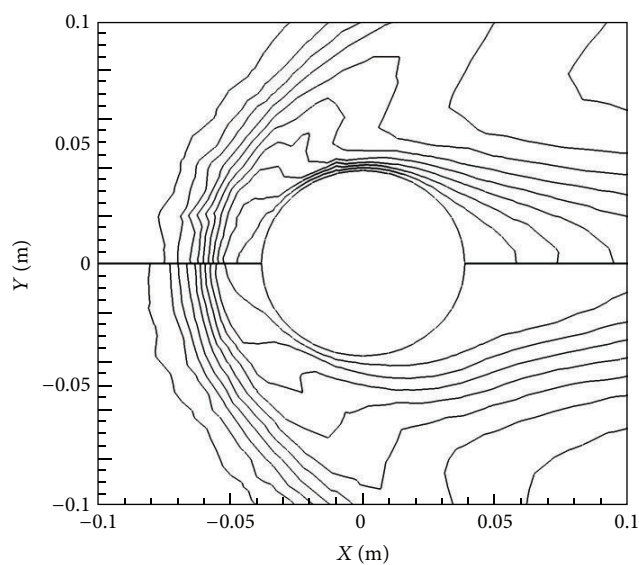


FIGURE 13: Comparison of U velocity contours without magnetic field (top) and with $B_{\max} = 2$ T oriented in Y -direction (bottom).

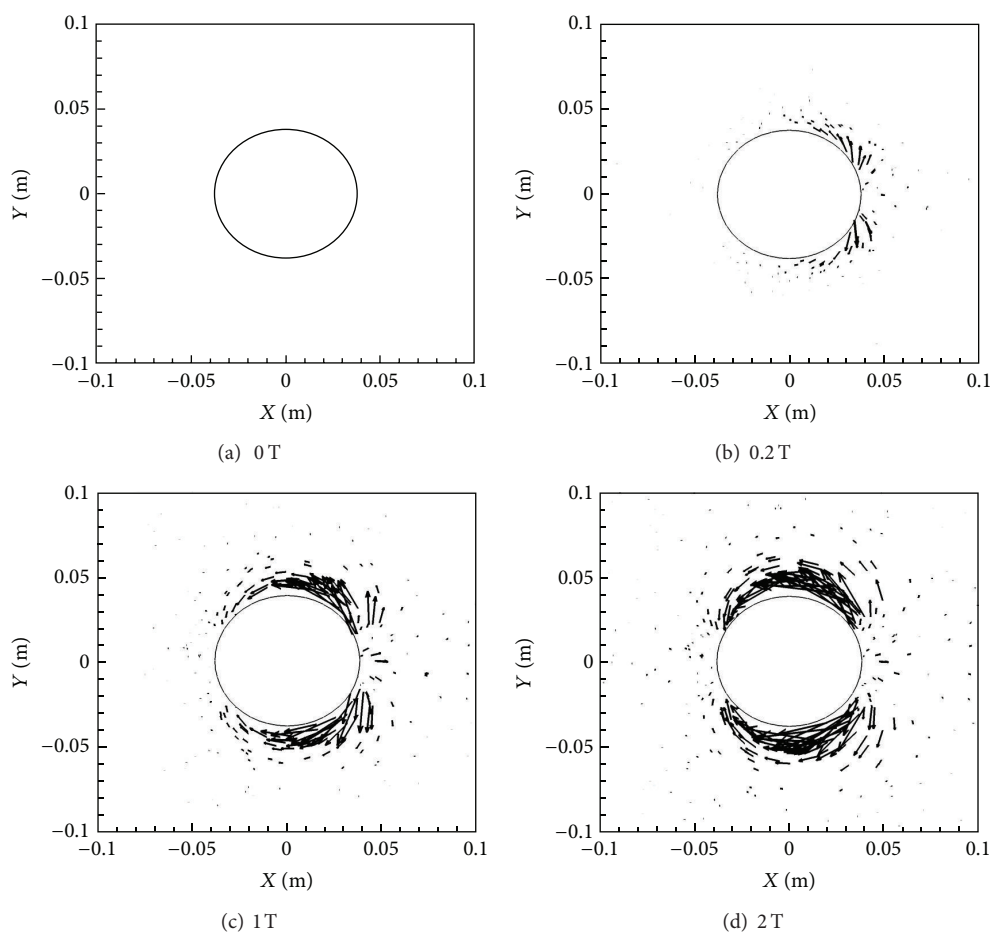


FIGURE 14: Lorentz force vectors for various B_{\max} with Y -orientation.

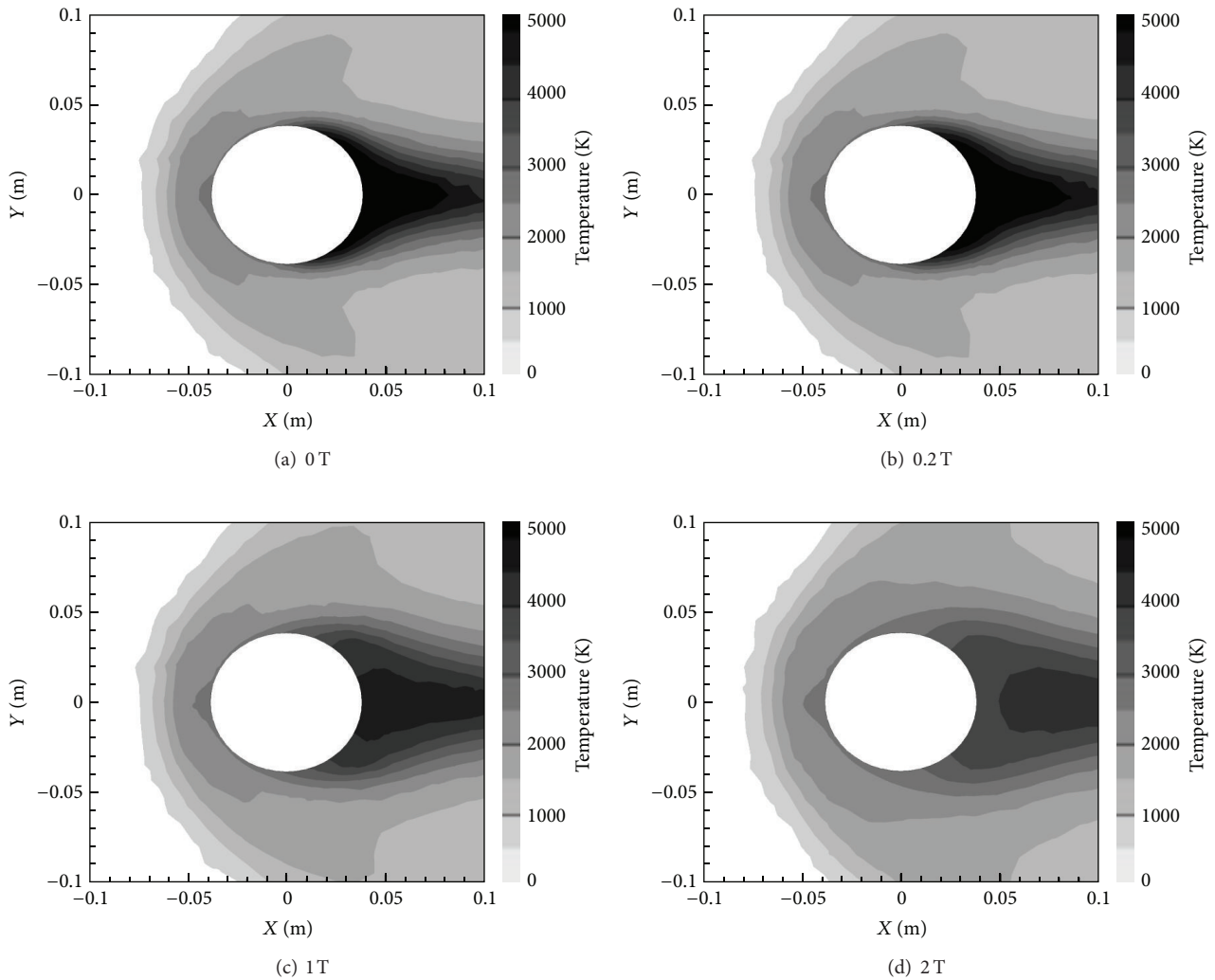


FIGURE 15: Temperature contours for various B_{max} with Y-orientation.

This change in location and direction of the Lorentz force predates practically all the flow changes between the two magnetic dipole orientations.

Figure 11 displays the vectors of velocity for the four cases. Here, too, the addition of the magnetic field causes a considerable change in flow patterns, which start to become increasingly obvious at the highest magnetic field case. In addition, the flow in the Y-oriented dipole cases is directed more in the transverse direction compared to the X-oriented dipole case, and this becomes only very obvious in the $B_{max} = 2\text{ T}$ case. This is primarily due to the Lorentz force effects being dominant on the top and bottom of the cylinder.

Figures 12 and 13 directly compare the velocity and density contours for the two cases $B_{max} = 0\text{ T}$ and 2 T . Here, in the same manner as with the X-oriented case, it is possible to directly see the influence of the Y-oriented magnetic field. Just as with the X-orientation, the influence of the magnetic field is starkly visible, as the contours of velocity and density are pushed out and away from the cylinder. Note, however, the increased effect in the Y-direction and slight decrease in

effect in the X-direction, in comparison to the X-oriented dipole cases. It is obvious that the velocity contours are being pushed out now in the transverse direction to the flow. This is due to the direction of the Lorentz force, which has now changed with the differing orientation of the magnetic field.

Figure 15 shows the temperature contours for the various B_{max} values. Similar to the X-oriented field, there is a demonstrable decrease in wall-adjacent temperature around the cylinder. However, this decrease is not quite as large as the drop in values manifested by the X-oriented field. A quantitative analysis of the reduction in temperature is provided in Table 1. The reduction in temperature is again due to the damping of flow velocities by the Lorentz force (see discussion above for the X-oriented field case). Figure 16 reveals the contours of Joule Heat for the Y-oriented magnetic dipole fields. Joule heat is now very low everywhere except along the top and bottom regions around the cylinder, this time, due to the Y-oriented magnetic field. There is an increase in the maximum Joule heat values compared to the X-oriented magnetic field, which is mainly because the

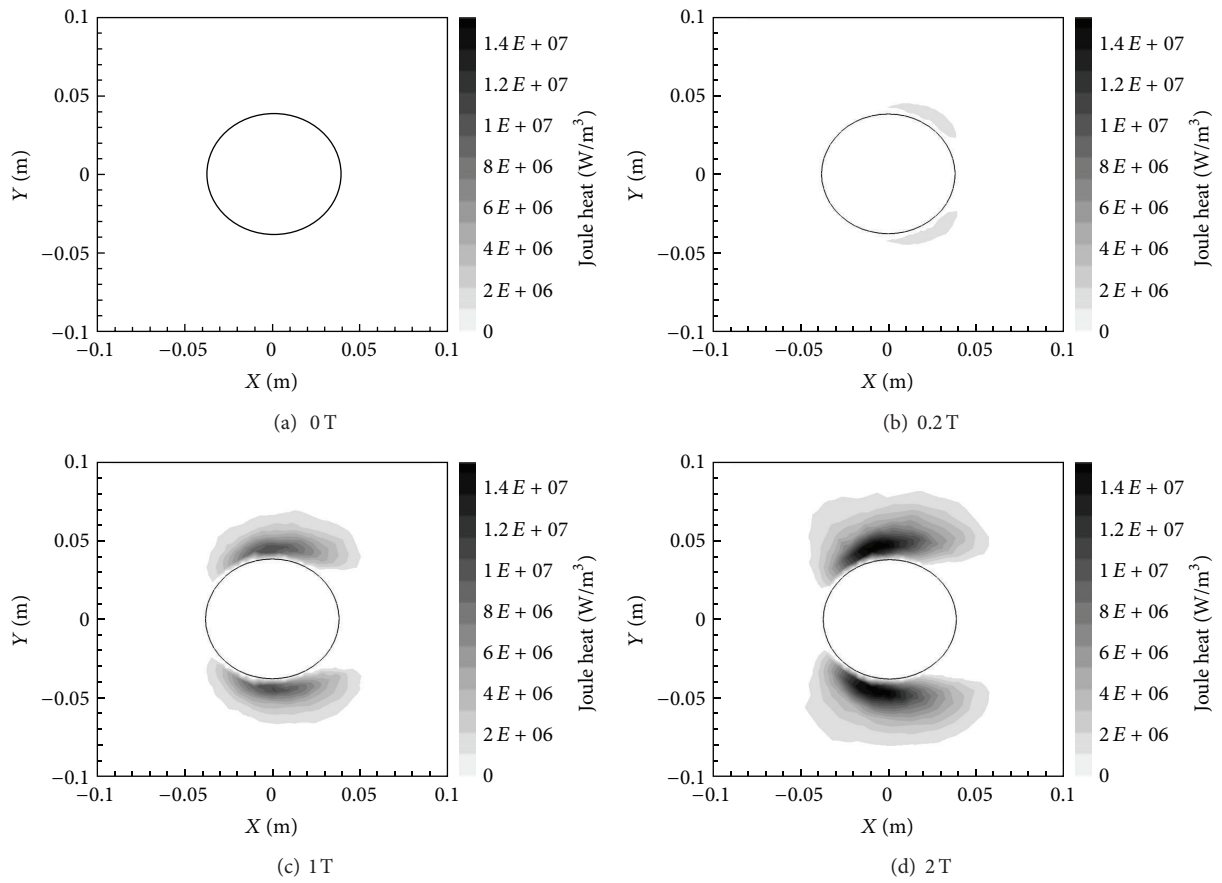


FIGURE 16: Joule heat contours for various B_{\max} with Y-orientation.

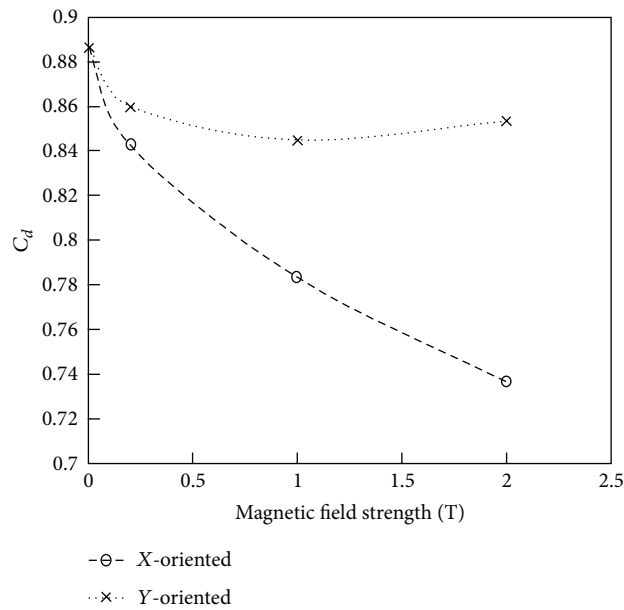


FIGURE 17: Comparison of drag coefficient for both X- and Y-oriented magnetic fields.

TABLE 1: Percent changes in C_d , average wall-adjacent temperature, and shock-standoff distance for various B_{\max} .

Case	C_d	Average wall-adjacent temperature	Shock distance
0.2 T X-oriented	-5.0%	-3.2%	0.14%
1 T X-oriented	-11.7%	-13.5%	1.5%
2 T X-oriented	-17.0%	-18.5%	5.4%
0.2 T Y-oriented	-3.0%	-1.1%	0.10%
1 T Y-oriented	-4.7%	-10.1%	1.2%
2 T Y-oriented	-3.7%	-17.5%	4.5%

region where electrical conductivity is the lowest (top and bottom) coincides with the region where the magnetic field or current density is the highest.

Lastly, we compare the effect that the magnetic field magnitudes and orientations have on the resulting drag coefficients, average wall-adjacent temperatures, and shock distance for all the cases. Figure 17 compares the drag coefficient and Table 1 illustrates quantitatively the effect of magnetic field and orientation on drag coefficient, average wall temperature, and shock-standoff distance. The percentage reductions in variables are calculated as

% change

$$= \frac{\text{Zero magnetic field value} - \text{Finite magnetic field value}}{\text{Zero magnetic field value}}. \quad (11)$$

From Figure 17, it is clear that the drag coefficient reduces for both orientations with increasing magnetic field. It is, however, observed that, for the Y-oriented field, C_d starts to increase for the highest magnetic field of 2 T. From Table 1 it can be seen that with an increase in magnetic field, both drag coefficient and the average wall-adjacent temperatures are progressively reduced and the shock-standoff distance is increased compared to the no-magnetic field case, although the percentage change in values is higher for the X-oriented dipole, especially for the drag coefficient where the X-oriented field results in four times the drag reduction. For the Y-oriented field, C_d starts to increase at higher magnetic fields because of an increase in pressure drag. This increase is mostly due to the significant reduction in flow velocities on the top and bottom of the cylinder (with the Y-oriented field being the strongest on the top and bottom), which eventually leads to increased pressures in these regions. The change in shock-standoff distance presented here is calculated as the distance between the discontinuities in density from the cases with and without magnetic field and it is observed that there is up to a 5.4% change in this distance with the X-oriented field.

Overall, it was observed that the X-oriented field resulted in stronger effects compared to the Y-oriented field at the same magnetic field strength, that is, effects in terms of reduction in flow velocities, overall temperatures, average wall temperatures, and drag coefficients. This is because the X-oriented field obviously has its strongest magnetic field strength in a direction aligned with the primary flow direction, which in turn means that the Lorentz force is also

aligned with this direction. Hence, the Lorentz force has its maximum influence for the X-oriented field case since it is primarily parallel to the direction of the flow, while, for the Y-oriented field case, it is perpendicular.

As mentioned in the beginning of this paper, there have been quite a few studies in this area over the last decade, and many of them demonstrated similar effects as the ones observed here. Particularly relevant to the current study is the work by Bisek et al. [23], who carried out a computational investigation of near-hypersonic flow of argon gas over a hemispherical body with a dipole magnetic field and noticed similar effects on shock-standoff distance. Utilizing several electrical conductivity models, they achieved up to approximately 16% increase in shock-standoff distance with $B_{\max} = 0.28$ T. Numerical and experimental work by Bityurin and coworkers [17, 35, 36] on flow over a cylinder also showed an increase in shock distance (up to a 45% increase with $B_{\max} = 0.45$ T), as well as a decrease in temperature around the cylinder with the application of a magnetic field. Gülhan et al. performed an experimental study on partially-ionized argon gas and found up to a 44% decrease in surface temperature [37]. Grigoriadis et al. [22] Shatrov and Gerbeth [27], and Zhang et al. [28] all demonstrated effects that magnetic field and Lorentz force can have on drag reduction and encountered varying degrees of effectiveness in reducing drag. Zhang et al., for instance, found the drag coefficient to decrease linearly, even into a negative drag coefficient, with increasing interaction parameter (analogous to increasing B_{\max}). This decrease was dependent on both the orientation and intensity of magnetic field strength, in line with our results. The comparatively lower magnitude that some of our results display in relation to previous studies (e.g., a 5.4% change in shock-standoff distance versus 45% noticed in [36]) can be attributed to the relatively lower electrical conductivity encountered in this study.

7. Conclusions

The effects of a magnetic field applied to partially ionized laminar hypersonic flow over a cylinder were considered in this paper. Boundary values and the properties of the ionized air were chosen to simulate the environment of earth's atmosphere at a height of 50,000 m. As the resulting flow was characterized by a low-magnetic Reynolds number, the MHD effects were distilled down to two source terms—the Lorentz force and Joule heat—which were added to the momentum and energy equations, respectively. These two variables drove the changes that occurred in the flow with the addition of

the magnetic field. Two magnetic fields, axial- and transverse-oriented dipoles, were compared.

The results show a decrease in flow velocities, especially behind the cylinder, decrease in flow temperature near the entire cylinder surface, an increase in the shock-standoff distance, and a decrease in the drag coefficient due to the damping effects of the Lorentz force. Effects increase with B_{\max} for the X -oriented field, while the Y -oriented field displays a lower overall effect, and in particular a lower decrease in reduction of the drag coefficient. These results are similar to findings of other researchers and add to the evidence of the benefits MHD can provide in future space vehicles. Future considerations include addressing transient and turbulent flows and further advances in weakly ionized atmospheric air electrical conductivity modeling.

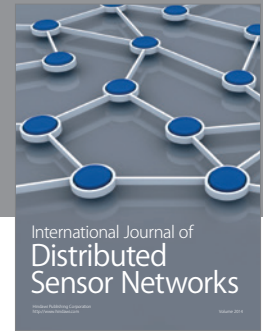
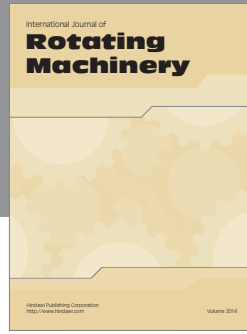
Nomenclature

N_A :	Avogadro constant
k :	Boltzmann's constant
L :	Characteristic length
ρ :	Mass density
D :	Diameter
μ :	Dynamic viscosity
Q :	Electron collision cross-section
e :	Electric charge
σ :	Electrical conductivity
n_e :	Electron number density
m_e :	Electron mass
J_H :	Joule heat
δ :	Kronecker delta function
F_{Lor} :	Lorentz force
η :	Magnetic diffusivity
μ_0 :	Magnetic permeability of free space
B_{\max} :	Max value of magnetic field
n :	Particle concentration
ϵ_0 :	Permeability of free space
p :	Pressure
h_{tot} :	Specific total enthalpy
T :	Temperature
λ :	Thermal conductivity
U :	Velocity vector
τ :	Viscous stress tensor.

References

- [1] J. Geffray, J.-P. Petit, and F. David, "MHD hypersonic flow control for aerospace applications," in *Proceedings of the 16th AIAA/DLR/DGLR International Space Planes and Hypersonic Systems and Technologies Conference*, AIAA-2009-7348, Bremen, Germany, October 2009.
- [2] C. Bruno, P. A. Czysz, and S. N. B. Murthy, "Electro-magnetic interactions in a hypersonic propulsion system," in *Proceedings of the 33rd AIAA/ASME/SAE/ASEE Joint Propulsion Conference*, AIAA-1997-3389, Seattle, Wash, USA, 1997.
- [3] D. I. Brichkin, A. L. Kuranov, and E. G. Sheikin, "Scramjet with MHD control under ajax concept. physical limitations," in *Proceedings of the 39th AIAA Aerospace Sciences Meeting and Exhibit*, AIAA-2001-0381, Reno, Nev, USA, January 2001.
- [4] J. Poggie and D. V. Gaitonde, "Magnetic control of flow past a blunt body: numerical validation and exploration," *Physics of Fluids*, vol. 14, no. 5, pp. 1720–1731, 2002.
- [5] I. V. Adamovich, J. W. Rich, S. J. Schneider, and I. M. Blankson, "Magnetogasdynamic power extraction and flow conditioning for a gas turbine," in *Proceedings of the 34th Plasmadynamics and Lasers Conference*, AIAA Paper 4289, pp. 2003–4289, 2003.
- [6] R. L. Kimmel, J. R. Hayes, J. A. Menart, and J. Shang, "Effect of magnetic fields on surface plasma discharges at mach 5," in *Proceedings of the 35th AIAA Plasma Dynamics and Lasers Conference*, AIAA Paper 2004-2661, 2004.
- [7] P. A. Davidson, *Introduction to Magnetohydrodynamics*, Cambridge University Press, New York, NY, USA, 2001.
- [8] P. A. Davidson, "Magnetohydrodynamics of materials processing," *Annual Review of Fluid Mechanics*, vol. 32, pp. 273–300, 1999.
- [9] A. R. Kantrowitz, "A survey of physical phenomena occurring in flight at extreme speeds," in *Proceedings of the Conference on High-Speed Aeronautics*, A. Ferri, N. J. Hoff, and P. A. Libby, Eds., pp. 335–339, 1955.
- [10] E. L. Resler and W. R. Sears, "The prospects for magneto-aerodynamics," *Journal of Aeronautical Sciences*, vol. 25, pp. 235–245, 1958.
- [11] W. B. Bush, "Magnetohydrodynamic-hypersonic flow past a blunt body," *Journal of Aerospace Sciences*, vol. 25, article 685, 1958.
- [12] W. B. Bush, "The stagnation-point boundary layer in the presence of an applied magnetic field," *Journal of Aerospace Sciences*, vol. 28, pp. 610–611, 1961.
- [13] J. F. Coakley and R. W. Porter, "Time-dependent numerical analysis of MHD blunt body problem," *AIAA Journal*, vol. 9, no. 8, pp. 1624–1626, 1971.
- [14] G. Palmer, "Magnetic field effects on the computed flow over a mars return aerobrake," *Journal of Thermophysics and Heat Transfer*, vol. 7, no. 2, pp. 294–301, 1993.
- [15] V. M. Fomin, P. K. Tretyakov, and J.-P. Taran, "Flow control using various plasma and aerodynamic approaches," *Aerospace Science and Technology*, vol. 8, no. 5, pp. 411–421, 2004.
- [16] J. S. Shang, S. T. Surzhikov, R. Kimmel, D. Gaitonde, J. Menart, and J. Hayes, "Mechanisms of plasma actuators for hypersonic flow control," *Progress in Aerospace Sciences*, vol. 41, no. 8, pp. 642–668, 2005.
- [17] V. Biturur, A. Bocharov, and J. Lineberry, *Mhd Flow Control in Hypersonic Flight*, 2005.
- [18] R. K. Agarwal and J. Augustinus, "Numerical simulation of compressible viscous mhd flows for reducing supersonic drag for blunt bodies," in *Proceedings of the American Physical Society, Division of Fluid Dynamics Meeting*, AIAA Paper 1999-0601, 1999.
- [19] V. Biturur, A. Bocharov, and J. Lineberry, "Mhd flow control studies: Analytical study of mhd flow interaction around a right circular cylinder in transverse hypersonic flow," in *Proceedings of the 33rd AIAA Plasmadynamics and Lasers Conference*, AIAA Paper 2002-2112, 2002.
- [20] G. Chen, J. B. Zhang, and C. H. Lee, *Numerical Investigation of Hypersonic Mhd Flows*, 2007.
- [21] J. P. Petit and J. Geffray, "Mhd flow-control for hypersonic flight," 2008.
- [22] D. G. E. Grigoriadis, I. E. Sarris, and S. C. Kassinos, "MHD flow past a circular cylinder using the immersed boundary method," *Computers and Fluids*, vol. 39, no. 2, pp. 345–358, 2010.

- [23] N. J. Bisek, J. Poggie, and I. D. Boyd, *Numerical Study of AMHD-Heat Shield*, 2010.
- [24] M. K. Lockwood, D. H. Petley, J. G. Matin, and J. L. Hunt, "Air-breathing hypersonic vehicles design and analysis methods and interactions," *Progress in Aerospace Sciences*, vol. 35, pp. 1–32, 1999.
- [25] C. Park, D. W. Bogdano, and U. B. Mehta, "Theoretical performance of a nonequilibrium mhd bypass scramjet," in *Proceedings of the 39th Aerospace Sciences Meeting and Exhibit*, vol. 35 of *AIAA paper 2001-0792*, 2001.
- [26] D. M. Van Wie, D. J. Risha, and C. F. Suchomel, "Research issues resulting from an assessment of technologies for future hypersonic aerospace systems," in *Proceedings of the 42nd AIAA Aerospace Sciences Meeting and Exhibit*, vol. 35, pp. 2004–1357, January 2004.
- [27] V. Shatrov and G. Gerbeth, "Magnetohydrodynamic drag reduction and its efficiency," *Physics of Fluids*, vol. 19, no. 3, Article ID 035109, 2007.
- [28] H. Zhang, B.-C. Fan, Z.-H. Chen, and Y.-L. Li, "Effect of the Lorentz force on cylinder drag reduction and its optimal location," *Fluid Dynamics Research*, vol. 43, no. 1, Article ID 015506, 2011.
- [29] B. Lebrun, *Theoretical study of shock wave annihilation around a at wing in hot supersonic argon flow with Lorentz forces [Ph.D. thesis]*, Aix Marseille University, Provence, France, 1987.
- [30] Earth atmosphere model.
- [31] G. W. Sutton and A. Sherman, *Engineering Magnetohydrodynamics*, Dover, 2006.
- [32] S. Chapman and D. Enskog, *The Mathematical Theory of Non-Uniform Gases*, Cambridge University Press, New York, NY, USA, 1958.
- [33] R. Kimmel, J. Hayes, C. Tyler, and J. Shang, "Performance of a low-density hypersonic magneto-aerodynamic facility," Tech. Rep., Air Vehicles Directorate; Air Force Research Laboratory, 2003.
- [34] S. Aithal, R. Munipalli, and V. Shankar, "Performance enhancement of highspeed inlets using mhd," Tech. Rep., HyperComp, 2004.
- [35] V. Batenin and V. Bityurin, "Mhd flow control," Tech. Rep., Institute of High Temperatures RAS, 2006.
- [36] V. A. Bityurin and A. N. Bocharov, "Ground MHD experiments in hypersonic flows," *High Temperature*, vol. 48, no. 6, pp. 874–880, 2010.
- [37] A. Gülhan, B. Esser, U. Koch et al., "Experimental verification of heat-flux mitigation by electromagnetic fields in partially-ionized-argon flows," *Journal of Spacecraft and Rockets*, vol. 46, no. 2, pp. 274–283, 2009.



Hindawi

Submit your manuscripts at
<http://www.hindawi.com>

